

Investigation of Plasmonic Detection of Human Respiratory Virus

Chandreyee Manas Das, Yan Guo, Lixing Kang, Ho-pui Ho, and Ken-Tye Yong*

The COVID-19 virus has been recently identified as a new species of virus that can cause severe infections such as pneumonia. The sudden outbreak of this disease is being considered a pandemic. Given all this, it is essential to develop smart biosensors that can detect pathogens with minimum time delay. Surface plasmon resonance (SPR) biosensors make use of refractive index (RI) changes as the sensing parameter. In this work, based on actual data taken from previous experimental works done on plasmonic detection of viruses, a detailed simulation of the SPR scheme that can be used to detect the COVID-19 virus is performed and the results are extrapolated from earlier schemes to predict some outcomes of this SPR model. The results indicate that the conventional Kretschmann configuration can have a limit of detection (LOD) of $2\text{E-}05$ in terms of RI change and an average sensitivity of $122.4 \text{ degRIU}^{-1}$ at a wavelength of 780 nm.

symptoms of this disease can range from mild cough, runny nose, sneezing, and running fever to severe lung congestion and pneumonia. The virus can spread by coming into close contact with infected people by being exposed to their phlegm or cough droplets or by coming in contact with infected surfaces. Because of the constant flow of people in and out of infected countries, the situation has become pandemic and there are more than 6 million confirmed cases to date. Thus, the WHO has announced this outbreak as a cause of global concern. Compared to other earlier serious coronavirus outbreaks in the past like Middle East respiratory syndrome coronavirus (MERS-CoV) in 2012 and severe acute respiratory syndrome coronavirus (SARS-CoV) in 2002, which had

1. Introduction

The last day of the year 2019 saw the sudden outbreak of many cases of pneumonia in Wuhan, situated in the Hubei province of China that seemed to be caused by an unknown bug. Later, it was found out that the pathogen was a unique strain of a coronavirus that was never seen before and they named it as COVID-19. To date, the number of confirmed and suspected cases have been exponentially rising and there have been no signs of relief. Coronaviruses belong to the family of Coronaviridae and other Nidovirales and can majorly be seen in humans and mammals. The

high mortality rates, the COVID-19 virus has a relatively lower death rate of 2%. However, the transmission rate of this particular newly found strain of virus is higher than the earlier viruses of the same family.^[1]


Acute respiratory diseases (ARD) are quite common and can affect children and adults of any age. Major viruses that have caused ARD include parainfluenza virus (PIV) type 1 (PIV1), PIV2, PIV3, PIV4, respiratory syncytial virus (RSV), influenza A and B viruses, bocavirus, adenovirus, rhinovirus, coronavirus (CoV), enterovirus, the newly discovered parvovirus types 4 and 5, and mimivirus. Rhinoviruses and CoVs have been affecting humans since the 1960s. However, until recently the medical fraternity never gave much attention to them since their impact was considered to be minor. CoVs can be fatal and in some cases they can cause severe lower respiratory tract infections (LRTI) and hence diagnostic testing to determine the pathogen becomes really important. Therefore, developing an efficient and reliable diagnostic system that can differentiate and distinguish among these pathogens is of paramount importance.^[2] **Table 1** below shows a list of several diagnostic methods that are used for detecting respiratory viruses and it also gives their drawbacks. The tests are mainly categorized into serological testing: hemagglutination inhibition assay (HI), complement fixation test and enzyme immunoassays like enzyme linked immunosorbent assay (ELISA); immunofluorescence: direct fluorescence antibody (DFA); and nucleic acid amplification Test (NAAT): reverse transcription polymer chain reaction (RT-PCR), qPCR, nucleic acid sequence-based amplification (NASBA), and loop-mediated isothermal amplification (LAMP). Serological testing determines the presence of any antibodies that result because of the presence

C. M. Das, L. Kang, Prof. K.-T. Yong
CINTRA CNRS/NTU/THALES, UMI 3288
Research Techno Plaza
50 Nanyang Drive, Border X Block, Singapore 637553, Singapore
E-mail: ktyong@ntu.edu.sg

C. M. Das, L. Kang, Prof. K.-T. Yong
School of Electrical and Electronic Engineering
Nanyang Technological University
50 Nanyang Avenue, Singapore 639798, Singapore

Y. Guo
School of Automation
Hangzhou Dianzi University
Hangzhou, Zhejiang 310018, China

Prof. H.-pui Ho
Department of Biomedical Engineering
The Chinese University of Hong Kong
New Territories, Hong Kong SAR 999077, China

 The ORCID identification number(s) for the author(s) of this article can be found under <https://doi.org/10.1002/adts.202000074>

DOI: 10.1002/adts.202000074

Table 1. Diagnostic methods of respiratory viruses.

S. No.	Genre of test	Current respiratory virus detection technique	Drawbacks	Signal measured
1.	Serological testing	Hemagglutination inhibition assay (HI) ^[2]	1) Low sensitivity and specificity	Agglutination level observed under microscope.
2.		Complement fixation test	1) Low sensitivity 2) Time-consuming 3) Non-specific	Presence of cell lysis of sheep red blood cells observed under microscope.
3.	Immunofluorescence	Enzyme immunoassays like Enzyme Linked Immunosorbent Assay (ELISA)	1) Expensive kits 2) Well-trained technicians required 3) False positive/negative results possible with mutated antigens	Absorbance values produced from the substrate-enzyme complex.
4.		Direct fluorescence antibody (DFA) ^[2]	1) Cross reactivity 2) Careful controls to ensure no false positives/negatives are present	Fluorescence observed under microscope
5.	Nucleic Acid Amplification Test (NAAT)	Reverse Transcription Polymer Chain Reaction (RT-PCR), qPCR ^[2]	1) Time-consuming 2) Trained analysts required 3) Systematic and careful collection, handling and transportation of specimen 4) Genetic variability of RNA can result in mismatches between primers and target sequences giving false negative results	Fluorescent signal from DNA binding dyes
6.		Nucleic acid sequence-based amplification (NASBA) ^[3]	1) High-quality RNA required 2) Maintenance of reaction temperatures up to 42° C 3) Target RNA sequence should have 120–150 nucleotides for optimal amplification	Fluorescent signal from molecular beacons attached to RNA.
7.		Loop-mediated isothermal amplification (LAMP) ^[4]	1) Proper design of primer 2) Less sensitive in case of complex samples like blood	Fluorescence values DNA binding dyes.

of the corresponding antigens obtained from being infected with the respective viruses. Immunofluorescence measures the fluorescence of a fluorescent dye that attaches to the antibody. NAAT amplifies the nucleic acids DNA or RNA and measures the fluorescent levels of dyes that attach to these amplified molecules.

The physics behind the concept of surface plasmon resonance (SPR) came into existence in the 1980s. Surface plasmons (SP) are formed as a result of interaction between electromagnetic (EM) light waves and nano-sized metals like gold (Au) or silver (Ag). Plasmon-based immunoassays have garnered a lot of attention in the field of biomolecular sensing. SPR-based assays have several advantages that can overcome the drawbacks and limitations of other conventional methods of testing. These assays rely on refractive index (RI) changes for detection of biomolecules and therefore they do not need any label. Since only small amount of sample sizes are required for testing, this technique can be very cost-effective. Additionally, commercial SPR machines can handle complex samples and hence it is not mandatory to have extremely pure high-quality samples if proper care is taken while sample injection through the microfluidic channels and the instrument is properly maintained by frequent regular clean-up of its internal components. Moreover, the results are repeatable and have high accuracy. In short, plasmonic detection technique offers label-free and real-time approach toward investigation of biomolecular reactions.^[5–18] **Table 2** shows some previously designed SPR schemes that have been used for detection of several viruses. It lists down the ligand molecules used for capturing

the viruses, the specific SPR scheme, the limit of detection (LOD), and the interrogation technique or the signal measured. There have been many SPR schemes where commercial sensing equipment have been used for detecting respiratory viruses like PlexArray HT system used for detecting viruses like Influenza A, Influenza B, H1N1, RSV; Spreeta SPR detector for detecting avian influenza virus (AIV) and Biacore T100 for detecting influenza virus.

SPR biosensors rely on the generation of surface plasma waves (SPW) for studying biomolecular interactions. SPWs are free electron density waves traveling across the metallic surface. It is crucial to have a plasmonic metal like gold (Au) or silver (Ag) that have large number of free electrons. These waves are excited by p-polarized light interacting with the electrons on the metallic surface. When the component of incident light wave vector (k_x) parallel to the surface matches with that of the SPW (k_{sp}), the resonance condition is achieved. It is not possible to generate SPWs by direct coupling of light with the smooth metal surface since the propagation constant of an SPW is greater than the incident light wave vector. With special arrangements like the attenuated total reflection (ATR) configuration, the two wave vectors can be matched. The conventional Kretschmann arrangement makes use of the ATR method for the excitation of SPs. The configuration consists of a high RI prism like SF10, SF11, or BK7 coated with a thin-film nano-sized plasmonic metal (Au or Ag) and is followed by a dielectric medium (air or water). The incoming light crosses the prism and gets total

Table 2. Earlier works on SPR-based detection of viruses.

S. No.	Name of virus	Capturing molecule	SPR scheme	Detection limit	Signal measured
1.	Plant virus coat proteins ^[19]	DNA aptamers	IBIS iSPR (IBIS Technologies BV, Hengelo, The Netherlands)	250 nm	Angular modulation
2.	Avian Influenza A H7N9 virus ^[20]	H7-mAb	Custom made Intensity modulated (IM) – SPR	402 copies/mL	Voltage measured in mV
3.	Multiple Respiratory Viruses (Influenza A, Influenza B, H1N1, RSV, PIV 1,2,3, Adenovirus, SARS CoV) ^[21]	Oligonucleotide probes	PlexArray HT system, Plexera Bioscience	Influ A—5 nm Influ B—1 nm PIV1—1 nm PIV2—2.5 nm PIV3—3.5 nm RSV—3 nm ADV—0.5 nm SARS—2 nm H1N1—3 nm	Angular modulation
4.	Avian Influenza Virus H1N1 ^[22]	DNA aptamers	Spreeta SPR detector, Texas Instruments	0.128 HAU	Angular modulation
5.	Anti-EBNA ^[23]	BSA-EBNA	Custom made WDM-SPR	1 pM	Wavelength modulation
6.	Cowpea Mosaic Virus ^[24]	Single chain variable fragment scFv molecules	Biacore X	12.5 μg mL ⁻¹	Angular modulation
7.	HIV-1 ^[25]	Streptavidin-biotin modified chips	Biacore 1000	16.6 μg mL ⁻¹	Angular modulation
8.	hHBV ^[26]	Anti-HBV	Spreeta SPR, Texas Instruments	9.2 nm	Angular modulation
9.	Avian Leucosis Virus ^[27]	mAb ALV-J	Custom made SPR waveguide immunosensor	—	Wavelength modulation
10.	Influenza virus ^[28]	α2-3 Sia glycan and α2-6 Sia glycan	Biacore T100	3.125 nm	Angular modulation

internally reflected at the prism base, where an evanescent wave is produced that penetrates the metal film. By varying the angle of incidence, the two wave vectors can be matched and the resonance condition can be achieved. This angle is known as the SPR angle and at this condition the reflected light has minimum intensity. Mathematically, this can be explained using Equations (1)–(3). In the Kretschmann arrangement, medium one is the glass prism, medium two is the plasmonic metal Au, and medium three is the analyte (de-ionized (D.I.) water). n_1 , n_2 , and n_3 represent the respective RI's of the three different media.^[6–10]

$$k_x = \frac{2\pi}{\lambda} \times n_1 \times \sin \theta_{\text{res}} \quad (1)$$

$$k_{\text{sp}} = \frac{2\pi}{\lambda} \times \sqrt{\frac{n_2^2 n_3^2}{n_2^2 + n_3^2}} \quad (2)$$

The resonance angle can be determined using Equations (1) and (2) above.

$$\theta_{\text{res}} = \sin^{-1} \text{Re} \left(\frac{1}{n_1} \sqrt{\frac{n_2^2 n_3^2}{n_2^2 + n_3^2}} \right) \quad (3)$$

The resonance angle varies with changes in RI of the analyte medium. When biomolecular ligand-analyte interactions occur at

the sensor surface, they cause small changes in the RI of the analyte layer. Thus, these small changes cause the SPR peak angular position (PAP) to shift. In commercial SPR sensors, the sensorgram displays the relative change in the SPR PAP in real time (response measured in resonance units (RU) vs time) that shows the binding interactions taking place on the sensor surface. A changing SPR angle gets depicted as a changing response signal in the sensorgram. Most commercially available SPR sensors make use of angular interrogation technique where the change in RI caused by analyte-ligand interaction causes a movement of the resonance angle. A change of 1000 RU in the response corresponds to 0.1° change in SPR angle.^[15–17]

There are many commercial SPR biosensor systems. Most of them operate at the far end of visible spectrum or at the beginning of near-infra red (NIR) region. Biacore 3000 operates at about 780 nm. SPRm 200 manufactured by Biosensing Instrument (BI) works at 690 nm and Spreeta 2000 developed by Texas Instruments Inc. uses an 830 nm light source. Thus, in this work we perform our simulation at these three wavelengths. In Section 2, we discuss about the simulation method with its mathematical details and the SPR sensing structure (both standard Kretschmann scheme and graphene modified layout). We discuss about the simulation results in Section 3 where we also present some electric field simulation data obtained using a software called COMSOL Multiphysics. Finally, in Section 4, we end with a concluding note.

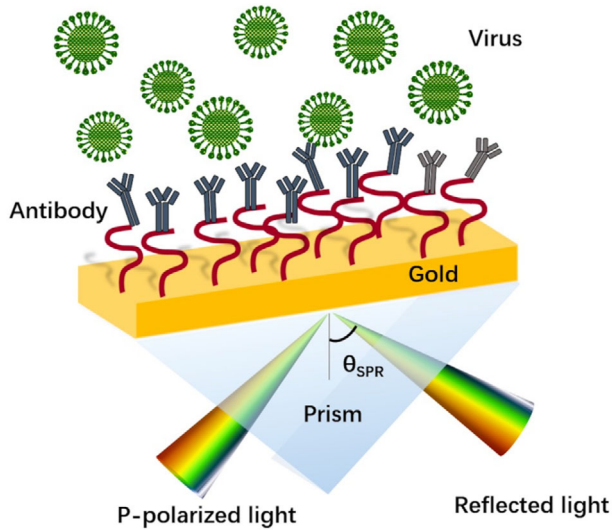


Figure 1. Schematic of SPR setup.

2. Structure, Equation, and Simulation Method

2.1. Sensor Structure

The basic SPR sensing scheme consists of 50 nm Au coated on a high RI glass prism. The reason behind choosing 50 nm Au is that the basic Kretschmann arrangement uses standard 50 nm Au and the commercial sensors available in the market too make use of this standard arrangement. Hence, we have three layers. BK7 prism forms the first layer. The plasmonic metal Au is the second layer and the analyte D.I. water acts as the third layer. Commercial sensors generally use buffer solutions as the analyte. For instance, Biacore 3000 uses hepes buffered saline (HBS) as the analyte. Since the RI of HBS is not very different from that of D.I. water, we believe that changing the analyte to running buffer solution will not cause a significant change in the simulation results. The sensing scheme has been depicted in **Figure 1**. To effectively capture the target pathogen molecule under test, it is essential to functionalize the Au surface using ligands like antibodies or aptamers. For instance, in ref. [21] the sensor surface was modified with oligonucleotide probes for detection of multiple respiratory viruses like Influenza A and B, PIV 1, 2, and 3. DNA aptamers were used for structural modification in case of AIV H1N1 detection.^[22] Biotin-streptavidin modified chips were used for HIV-1 detection.^[25] We also perform additional simulation on graphene modified SPR scheme. In this case, we add N_{gh} layers of 0.34 nm graphene between Au and the analyte. Hence, there are total four layers in this modified layout where graphene is now the third layer and the analyte forms the fourth layer.

2.2. Mathematical Equations

We use Fresnel's equations [Transfer matrix method (TMM)] for calculating the reflectivity of the multi-layer SPR structure.

$$M = \prod_{k=2}^{N-1} M_k$$

where

$$M_k = \begin{bmatrix} \cos \beta_k & \frac{-i \sin \beta_k}{q_k} \\ -i q_k \sin \beta_k & \cos \beta_k \end{bmatrix} \quad (4)$$

$$q_k = \frac{(\epsilon_k - n_1^2 \sin^2 \theta_1)^{\frac{1}{2}}}{\epsilon_k} \quad (5)$$

$$\beta_k = \frac{2\pi d_k}{\lambda} ((\epsilon_k - n_1^2 \sin^2 \theta_1)^{\frac{1}{2}}) \quad (6)$$

$$r_p = \frac{(M_{11} + M_{12} q_N) q_1 - (M_{21} + M_{22} q_N)}{(M_{11} + M_{12} q_N) q_1 + (M_{21} + M_{22} q_N)} \quad (7)$$

$$R_p = |r_p|^2 \quad (8)$$

$$S = \frac{d\theta_{SPR}}{dn_{bio}} \quad (9)$$

Elaborating on the different variables found in Equations (4) through (9), the total number of layers is denoted by N . λ represents the incident light wavelength and the RI and dielectric constant of the k th layer are given by n_k and ϵ_k respectively. Also, $\epsilon_k = (n_k)^2$. The thickness of the k th layer is given by d_k and θ_1 denotes the p-polarized light incident angle. R_p represents the reflectivity, θ_{SPR} denotes the angle of minimum reflectivity, n_{bio} is the RI of the analyte, and S is the angular sensitivity. M denotes the characteristic matrix of the N -layer system used in the TMM. The RI of BK7 prism, graphene, and the dielectric constant of Au can be found in refs. [29–31]. The respective RI and dielectric constant of these layers at different wavelengths have been provided in Table S1, Supporting Information. The RI of D.I. water has been considered to be 1.33. The thickness of the metallic layer is considered to be 50 nm. For graphene, $d_{gh} = N_{gh} \times t_{gh}$ (where t_{gh} is the thickness of one layer of graphene and it is taken to be equal to 0.34 nm and N_{gh} , d_{gh} denote the total graphene layers and the total thickness, respectively).

2.3. Simulation Technique

We perform the simulations at $\lambda = 690, 780, \text{ and } 830 \text{ nm}$. We vary the RI of the analyte layer n_{bio} from $1E-5$ to $1.1E-3$ in steps of $1E-6$ and calculate the sensitivity using Equation (6). For the graphene modified structure, we first optimize N_{gh} and arrive at a configuration that gives us maximum sensitivity. For calculating the sensitivity here, we take $\Delta n_{bio} = 0.005$. Next, for the optimized scheme, we vary the RI of the analyte layer from $5E-6$ to $1.1E-3$ in steps of $1E-6$ and calculate the sensitivity.

3. Results and Discussion

We perform the simulations at three different working wavelengths of commercial biosensors: SPRm200—690 nm, Biacore 3000—780 nm, and Spreeta 2000—830 nm. **Figure 2** below shows the basic SPR reflectivity curve, which is basically the variation of reflectivity, the ratio of intensities of reflected and incident

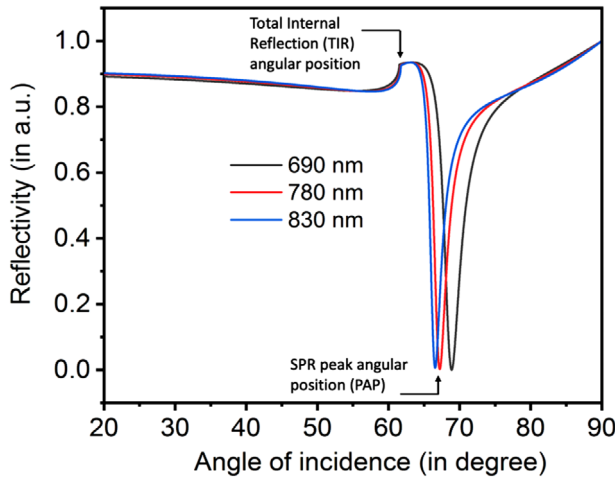


Figure 2. SPR reflectivity curve.

lights, with the angle of incident light. Since the prism has a high RI, the incident light experiences total internal reflection (TIR) for angles larger than the critical angle. When the incident angle exceeds the critical angle, a drop in the reflectivity is observed. At the SPR angle, the reflectivity is minimum and beyond this resonance angle, the reflectivity again starts increasing with an increase in the incident angle. The respective SPR angles at different wavelengths are: 690 nm—68.88°, 780 nm—67.21°, and 830 nm—66.56°.

Our simulation is based on data available from previous experiment works done by Bai et al.^[22] and Suenaga et al.^[28] In ref. [22], the researchers designed a SPR scheme to detect AIV H1N1. They used DNA aptamers to capture the virus. The captured AIV H1N1 molecules caused a rise in RI. We specifically make use of the calibration curve that relates virus concentrations [hemagglutination units (HAU)] to changes in RI. The AIV H1N1 has been used since the calibration curve directly relates virus concentration with change in RI. Since the concentration is not in specific molar units, the simulation cannot provide a specific molar detection limit. However, the simulation can provide a generic idea in broad terms on the possibility of using SPR scheme in the future. Table 2 provides details on several respiratory viruses that have been detected using the SPR scheme. The SPR scheme was able to detect a minimum of 2 nM of the SARS CoV (S. No. 3 in Table 2).^[21] Although, the COVID-19 and SARS viruses are quite different in nature, they belong to the same coronavirus family. Thus, given the fact that the SPR scheme was able to successfully detect low concentration of the SARS CoV, it gives us hope that the same plasmonic sensing scheme can be optimistically used to detect the COVID-19 virus. However, the exact detection limit is unknown and can only be assured after the design of a practical SPR layout. In ref. [28], the researchers modified the sensor surface with α -2-3 Sia glycan and α -2-6 Sia glycan to capture hemagglutinin (HA) proteins derived from AIV. Using Biacore T100, they could detect different concentrations of HA protein of A/H5N1/Vietnam/1203/2004. We make use of the sensorgram response curve that displays real-time data. For the pure Au Kretschmann layout, we vary the RI of analyte from 1E-5 to 1.1E-3 in steps of 1E-06. Figure 3 below gives the variation curve of sen-

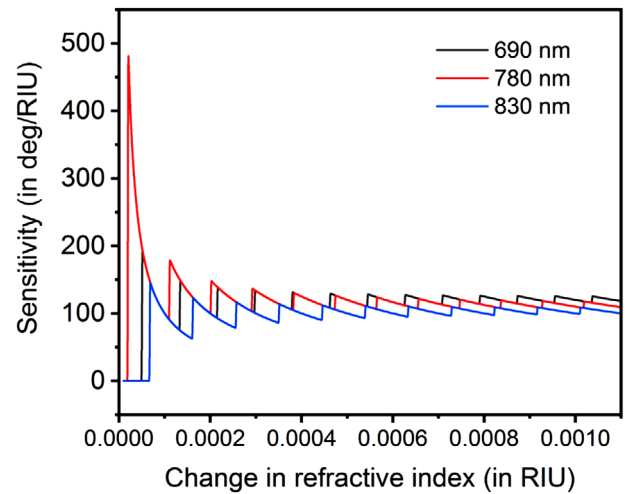


Figure 3. Sensitivity variation with changes in RI of the analyte for Kretschmann configuration.

sitivity versus change in RI for the three wavelengths. The minimum detection limits in terms of change in RI are: 690 nm—5.1E-5, 780 nm—2E-5, and 830 nm—6.8E-5. Using Equation (3), we can write the sensitivity as below in Equation (10). The relation between sensitivity and change in RI is complex and the nature is quite non-linear. The resulting sensitivity at a particular change in RI is the ratio of change in resonance angle to change in RI, and since change in resonance angle is also a function of change in RI, the resultant ratio does not follow a set pattern. At different wavelengths the values of n_1 and n_2 change. It is the cumulative result of n_1 , n_2 , and Δn_3 that lead to the sensitivity value at a particular wavelength. The relation is not simple and thus we do not observe a general trend with changing wavelengths.

$$S = \frac{\left[\begin{array}{c} \text{abs} \left(\sin^{-1} \text{Re} \left(\frac{1}{n_1} \sqrt{\frac{n_2^2 n_3^2}{n_2^2 + n_3^2}} \right) \right) \\ - \sin^{-1} \text{Re} \left(\frac{1}{n_1} \sqrt{\frac{n_2^2 (n_3 + \Delta n_3)^2}{n_2^2 + (n_3 + \Delta n_3)^2}} \right) \end{array} \right]}{\Delta n_3} \quad (10)$$

Using the calibration curve for AIV H5N1 detection, we calculate the respective concentration of virus in HAU with the help of the equation below given in ref. [22]. The respective values of HAU concentrations at these minimum RI values for the three wavelengths are: 690 nm – 0.0669 HAU, 780 nm – 0.033 HAU, and 830 nm – 0.0855 HAU. The maximum sensitivities at these wavelengths are: 690 nm –196.07 degRIU⁻¹, 780 nm – 500 degRIU⁻¹, and 830 nm – 147.05 degRIU⁻¹ and the average sensitivity values are: 690 nm –114.88 ± 25.48 degRIU⁻¹, 780 nm – 122.4 ± 38.68 and 830 nm – 95.8 ± 24.69 . The average sensitivity has been arrived by considering the sensitivity values at RI changes from 1E-05 to 1.1E-03. Using the definition in ref. [22]

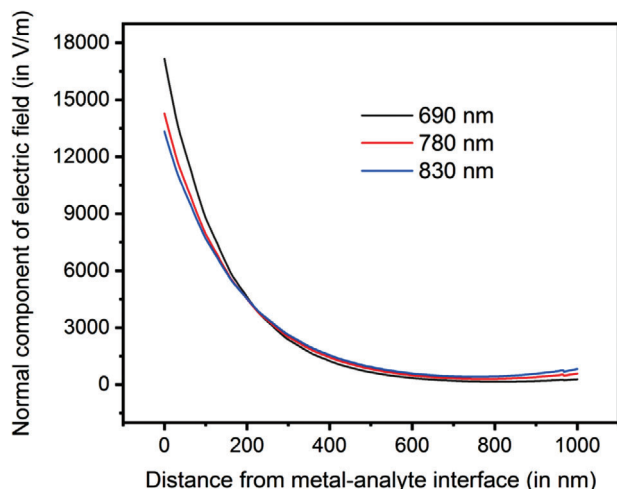


Figure 4. Variation of normal component of electric field with the distance from the metal-dielectric interface.

one HAU corresponds to a concentration of virus that is capable of completely agglutinating the red blood cells.

$$\gamma (\text{R.I. change}) = 915.6x (\text{concentration in HAU}) - 10.285 \quad (11)$$

Using Equation (11), the corresponding RI change for one HAU is 0.000905. In case of our SPR layout, since the HAU concentrations at these wavelengths are much below one HAU, we can argue that the SPR-based biosensor can safely detect the minimum toxicity level. As seen from Figure 3, the sensitivity values are high at low RI changes. This aspect can be really beneficial since biomolecular detection of nano and micro molecules like viruses and bacteria result in small RI changes. Thus, having a high sensitivity value at low RI change of analyte will enable easier detection of pathogens.

SPWs are EM waves traveling on the metal-dielectric interface. These waves have two components, one parallel to the surface of the metal and the other in the direction normal to it. The normal component of electric field is maximum at the sensor surface and it decreases exponentially as we move toward the analyte region. The field soon vanishes after traveling about one-third to half wavelength distance. The penetration depth, L_p , is the distance at which the field becomes e^{-1} of its value at the surface.^[32–34] Figure 4 displays the variation between the normal part of the electric field and the distance from the metal-dielectric interface. The penetration depth of this field at the three wavelengths are: 690 nm – 150.62 nm, 780 nm – 170.96 nm, and 830 nm – 183.71 nm. Biomolecular interactions that occur within this penetration depth are able to cause RI changes of the analyte and thus these interactions can then be detected. Figure S1, Supporting Information, shows a pictorial representation of the normal component of electric field along the entire sensor surface. The evanescent nature of this field can be easily seen.^[33]

2D materials constitute a fresh category of materials that possess some remarkable physical, optical, and chemical properties. Among these materials, graphene can offer several benefits in SPR-based sensing. Graphene can contribute to significant boost in the electric field at the substrate interface that can

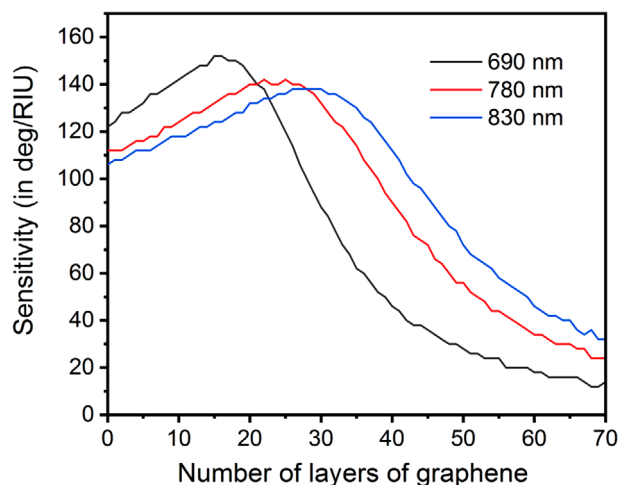


Figure 5. Variation of sensitivity as a function of number of graphene layers.

lead to higher sensitivity because of increased plasmon generation. Additionally, they have a large surface area of about $2630 \text{ m}^2 \text{ g}^{-1}$ and thus can have greater interaction with the analyte. They can selectively attach to aromatic compounds through pi-pi interactions.^[14,35–37] Hence, graphene can easily capture small biomolecules with this specific pi-pi bonding that they can form with the flowing analyte. Non-specific binding can cause major issues as it can lead to erroneous sensorgram curves. The non-specific binding sites can be blocked by using polyethylene glycol as a blocking agent.^[38] Apart from these features, graphene can now be commercially fabricated and is not just limited to research laboratories in universities. The coating of graphene over gold is also a known procedure and can be performed at a mass scale in industry. Several graphene-based schemes have been reported by various researchers. For instance, in ref. [39], the researchers were able to detect DNA hybridization events in attomolar concentration range with graphene-coated SPR interfaces. In another similar biomolecular detection scheme, researchers were able to detect low concentrations of microRNA and other molecules like adenosine using standard SPR substrate modified by graphene oxide-gold nanoparticles.^[40] Thus, we further analyze the graphene modified SPR configuration to have a detailed look into the enhancement in sensitivity and detection limits that it can give us.

For the Au + graphene layout, we first optimize N_{gh} . Using Equations (4) through (9), we evaluate the sensitivity for this modified layout. Figure 5 shows the sensitivity change as a function of graphene layers. We can observe a general trend here. The sensitivity increases as the graphene layers increase up to a specific limit beyond which the sensitivity starts falling down. With added graphene layers, there is enhanced light-matter coupling that enables more SPs to be produced and thus the sensitivity multiplies. However, when the number of graphene layers exceeds a certain value, the effect is counterproductive as it causes the incident photons to get absorbed because of which less photons are able to interact with the plasmonic metal causing reduced generation of plasmons. The number of layers of graphene that gives us the highest sensitivity is our optimized condition. The

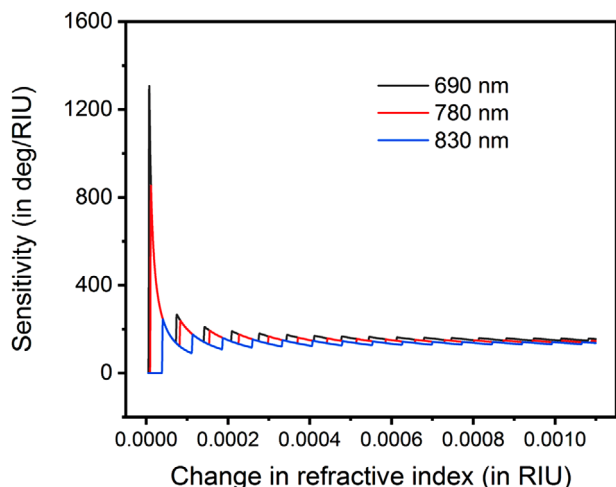


Figure 6. Sensitivity variation with changes in RI of the analyte for Au + graphene layout.

optimized condition for the three wavelengths are: 690 nm – 15 layers, 780 nm – 22 layers, and 830 nm – 26 layers.

In the modified Au + graphene layout, we vary the RI of analyte from $5E-6$ to $1.1E-3$ and observe the sensitivity. **Figure 6** below displays the variation of sensitivity with changes in the RI of the analyte for the graphene modified SPR layout. The minimum detection limits for the Au + graphene configuration in terms of change in RI are: 690 nm— $7E-6$, 780 nm— $1.1E-5$, and 830 nm— $4E-5$. Also, the respective values of HAU concentrations at these minimum RI values for the three wavelengths are: 690 nm—0.0188 HAU, 780 nm—0.023 HAU, and 830 nm—0.054 HAU; the maximum sensitivities at these wavelengths are: 690 nm— $1428.6 \text{ degRIU}^{-1}$, 780 nm— $909.09 \text{ degRIU}^{-1}$, and 830 nm— 250 degRIU^{-1} ; and the average sensitivity values are: 690 nm— 172.04 ± 86.04 , 780 nm— 156.93 ± 60.63 , and 830 nm— 132.17 ± 27.75 . If we compare the Au + graphene layout with the standard Kretschmann configuration, the detection limits are lowered by $4.4E-5$ @ 690 nm, $9E-6$ @ 780 nm, $2.8E-5$ @ 830 nm and the average sensitivities are enhanced 1.49 times @ 690 nm, 1.28 times @ 780 nm, 1.37 times @ 830 nm.

For both only Au configuration and Au + graphene layout, at the maximum sensitivity data point, the change in SPR angle is 0.01° for all wavelengths. For commercial sensors, a 1000 RU change in the response corresponds to a shift of 0.1° .^[15] Thus, for our case, this corresponds to a change of 100 RU. Using the real-time response curve of detection of HA protein of Suenaga et al.^[28] we develop a relation between concentration level and change in response in RIU. Figure S2, Supporting Information, displays this relation. We fit a logarithmic curve to the data points.

$$Y = 119.18 \ln(X) - 53.188 \quad (12)$$

Equation (12) shows the logarithmic relation between concentration of virus in nm (X) and change in response in RU (Y). A 100 RU change correlates to a concentration of 3.615 nm. Table 2 lists the detection limits for SPR detection of several respiratory viruses. The detection limits are: Influenza A—5 nm, Influenza B—1 nm, PIV1—1 nm, PIV2—2.5 nm, PIV3—3.5 nm, RSV—

3 nm, ADV—0.5 nm, SARS—2 nm, and H1N1—3 nm.^[21] Considering these limits, we can argue that 3.615 nm is a reasonable value obtained as the detection limit from the simulation.

4. Conclusion

Plasmon-based biosensors are rapidly evolving as a label-free and real-time bio-physical detection technique capable of giving accurate and reliable results in a quick span of time. The unanticipated breakdown of the contagious COVID-19 virus has claimed many lives and has jeopardized the entire world. In this work, we basically demonstrated with the help of simulation that SPR-based biosensors can serve as an important tool for detection of respiratory viruses. We performed the simulation at three different operating wavelengths of some commercially available SPR sensors. With actual data from previous real-time biomolecular SPR experiments on detection of AIV we performed simulation at 690, 780, and 830 nm for Au and Au + graphene layout and arrived at some key sensitivity and detection limit values. The Au layout gives a minimum LOD of $2E-5$ and a maximum sensitivity of 500 degRIU^{-1} at 780 nm. For the Au + Graphene configuration, the detection limit and sensitivity values are $7E-6$ and $1428.6 \text{ degRIU}^{-1}$ respectively at 690 nm. Additionally, using the experimental work done by Suenaga et al.,^[28] we developed a relation between concentration level and change in response in RIU. We found out that the SPR scheme can detect 3.615 nm of virus concentration. Hence, in clinical terms we can argue that the SPR scheme can detect concentration in the nm range.

Supporting Information

Supporting Information is available from the Wiley Online Library or from the author.

Acknowledgements

This work was supported by the Singapore National Research Foundation (NRF) and French National Research Agency (ANR), grant number (NRF2017-ANR002 2DPS).

Conflict of Interest

The authors declare no conflict of interest.

Keywords

COVID-19, graphenes, kretschmann layout, plasmonic bio-sensing, simulations

Received: April 8, 2020
Revised: May 14, 2020
Published online: June 8, 2020

- [1] C. Huang, Y. Wang, X. Li, L. Ren, J. Zhao, Y. Hu, L. Zhang, G. Fan, J. Xu, X. Gu, Z. Cheng, T. Yu, J. Xia, Y. Wei, W. Wu, X. Xie, W. Yin, H. Li, M. Liu, Y. Xiao, H. Gao, L. Guo, J. Xie, G. Wang, R. Jiang, Z. Gao, Q. Jin, J. Wang, B. Cao, *Lancet* **2020**, 395, 497.
- [2] J. B. Mahony, *Clin. Microbiol. Rev.* **2008**, 21, 716.
- [3] Md. Fakruddin, R. M. Mazumdar, A. Chowdhury, K. S. B. Mannan, *Int. J. Life Sci. Pharma Res.* **2012**, 2, 106.
- [4] P. R. Sahoo, K. Shetty, S. Mohapatra, D. Panda, *Vet. World* **2016**, 9, 465.
- [5] J. Homola, S. S. Yee, D. Myszka, in *Optical Biosensors: Today and Tomorrow*, 2nd ed. (Eds: F. S. Ligler, C. R. Taitt), Elsevier, Amsterdam **2008**, 185–242.
- [6] A. Verma, A. Prakash, R. Prakash, *Optik* **2016**, 127, 1787.
- [7] A. J. Tudos, R. B. M. Schasfoort, in *Handbook of Surface Plasmon Resonance* (Eds: R. B. M. Schasfoort, A. J. Tudos), Royal Society of Chemistry, Cambridge **2008**, 1–14.
- [8] R. P. H. Kooyman, in *Handbook of Surface Plasmon Resonance*, (Eds: R. B. M. Schasfoort, A. J. Tudos), Royal Society of Chemistry, Cambridge **2008**, 15–34.
- [9] N. A. Cinel, S. Bütün, E. Özbay, *Opt. Express* **2012**, 20, 2587.
- [10] E. Gorodkiewicz, Z. Lukaszewski, *Biosensors* **2018**, 8, 132.
- [11] B. S. Gao, N. Koshizaki, H. Tokuhisa, E. Koyama, T. Sasaki, J. W. Kim, J. Ryu, D. S. Kim, Y. Shimizu, *Adv. Funct. Mater.* **2010**, 20, 78.
- [12] R. B. M. Schasfoort, A. McWhirter, in *Handbook of Surface Plasmon Resonance*, (Eds: R. B. M. Schasfoort, A. J. Tudos), Royal Society of Chemistry, Cambridge **2008**, 35–80.
- [13] Q. Ouyang, S. Zeng, L. Jiang, L. Hong, G. Xu, X. Q. Dinh, J. Qian, S. He, J. Qu, P. Coquet, K.-T. Yong, *Sci. Rep.* **2016**, 6, 28190.
- [14] S. Zeng, S. Hu, J. Xia, T. Anderson, X. Q. Dinh, X. M. Meng, P. Coquet, K.-T. Yong, *Sens. Actuators, B* **2015**, 207, 801.
- [15] D. R. Shankaran, N. Miura, *J. Phys. D: Appl. Phys.* **2007**, 40, 7187.
- [16] K. V. Gobi, H. Iwasaka, N. Miura, *Biosens. Bioelectron.* **2007**, 22, 1382.
- [17] N.-F. Chiu, T.-Y. Huang, H.-C. Lai, K.-C. Liu, *Nanoscale Res. Lett.* **2014**, 9, 445.
- [18] Biacore, in *Biacore Sensor Surface Handbook*, GE Healthcare, Buckinghamshire, UK **2003**, pp. 1–7.
- [19] G. Lautner, Z. Balogh, V. Bardoczy, T. Meszaros, R. E. Gyurcsanyi, *Analyst* **2010**, 135, 918.
- [20] Y. F. Chang, W. H. Wang, Y. W. Hong, R. Y. Yuan, K. H. Chen, Y. W. Huang, P. L. Lu, Y. H. Chen, Y. M. A. Chen, L. C. Su, S. F. Wang, *Anal. Chem.* **2018**, 90, 1861.
- [21] L. Shi, Q. Sun, J. He, H. Xu, C. Liu, C. Zhao, Y. Xu, C. Wu, J. Xiang, D. Gu, J. Long, H. Lan, *Bio-Med. Mater. Eng.* **2015**, 26, S2207.
- [22] H. Bai, R. Wang, B. Hargis, H. Lu, Y. Li, *Sensors* **2012**, 12, 12506.
- [23] H. Vaisocherova, K. Mrkova, M. Piliarik, P. Jinoch, M. Steinbachova, J. Homola, *Biosens. Bioelectron.* **2007**, 22, 1020.
- [24] L. Torrance, A. Ziegler, H. Pittman, M. Paterson, R. Toth, I. Eggleston, *J. Virol. Methods* **2006**, 134, 164.
- [25] N. Bianchi, C. Rutigliano, M. Tomassetti, G. Feriotta, F. Zorzato, R. Gambari, *Clin. Diagn. Virol.* **1997**, 8, 199.
- [26] J. W. Chung, S. D. Kim, R. Bernhardt, J. C. Pyun, *Sens. Actuators, B* **2005**, 111–112, 416.
- [27] J. G. Huang, C. L. Lee, H. M. Lin, T. L. Chuang, W. S. Wang, R. H. Juang, C. H. Wang, C. K. Lee, S. M. Lin, C. W. Lin, *Biosens. Bioelectron.* **2006**, 22, 519.
- [28] E. Suenaga, H. Mizuno, P. K. R. Kumar, *Virulence* **2012**, 3, 464.
- [29] SCHOTT Zemax catalog, <http://www.schott.com> (accessed: January 2017).
- [30] J. W. Weber, V. E. Calado, M. C. M. van der Sanden, *Appl. Phys. Lett.* **2010**, 97, 091904.
- [31] A. K. Sharma, B. D. Gupta, *J. Appl. Phys.* **2007**, 101, 093111.
- [32] J. Renger, S. Grafström, L. M. Eng, *J. Opt. Soc. Am. A* **2004**, 21, 1362.
- [33] S. Ekgasit, C. Thammacharoen, F. Yu, W. Knoll, *Anal. Chem.* **2004**, 76, 2210.
- [34] C. Schlachter, F. Lisdat, M. Frohme, V. A. Erdmann, Z. Konthur, H. Lehrach, J. Glökler, *Biosens. Bioelectron.* **2012**, 31, 571.
- [35] F. H. L. Koppens, T. Mueller, P. Avouris, A. C. Ferrari, M. S. Vitiello, M. Polini, *Nat. Nanotechnol.* **2014**, 9, 780.
- [36] Z. Sun, A. Martinez, F. Wang, *Nat. Photonics* **2016**, 10, 227.
- [37] A. N. Grigorenko, M. Polini, K. S. Novodolov, *Nat. Photonics* **2012**, 6, 749.
- [38] S. Kaushik, U. K. Tiwari, A. Deep, R. K. Sinha, *Sci. Rep.* **2019**, 9, 6987.
- [39] O. Zagorodko, J. Spadavecchia, A. Y. Serrano, I. Larroulet, A. Pesquera, A. Zurutuza, R. Boukherroub, S. Szunerits, *Anal. Chem.* **2014**, 86, 11211.
- [40] Q. Li, Q. Wang, X. Yang, K. Wang, H. Zhang, W. Nie, *Talanta* **2017**, 174, 521.